International Journal of Heat and Mass Transfer 52 (2009) 345–354

Contents lists available at ScienceDirect

International Journal of Heat and Mass Transfer

journal homepage: www.elsevier.com/locate/ijhmt

Waviness effect of a wavy circular cylinder on the heat transfer at a Reynolds number of 300

C.T. Ahn [a], H.S. Yoon [b], M.Y. Ha [a,*], H.G. Lee [a]

[a] School of Mechanical Engineering, Pusan National University, San 30, Jangjeon Dong, Geumjeong Gu, Busan 609-735, Republic of Korea
[b] Advanced Ship Engineering Research Center, Pusan National University, San 30, Jangjeon Dong, Geumjeong Gu, Busan 609-735, Republic of Korea

ARTICLE INFO

Article history:
Received 30 August 2007
Received in revised form 31 May 2008
Available online 27 July 2008

ABSTRACT

The present study investigates three-dimensional characteristics of fluid flow and heat transfer around a wavy cylinder which has the sinusoidal variation in the cross sectional area along the spanwise direction. The three different wavelengths of $\pi/4$, $\pi/3$ and $\pi/2$ at the fixed wavy amplitude of 0.1 have been considered to investigate the effect of waviness on especially the forced convection heat transfer around a wavy cylinder when the Reynolds and Prandtl numbers are 300 and 0.71, respectively. The numerical solution for unsteady forced convective heat transfer is obtained using the finite volume method. The immersed boundary method is used to handle the wavy cylinder in a rectangular grid system. The present computational results for a wavy cylinder are compared with those for a smooth cylinder. The fluid flow and heat transfer around the wavy cylinder depends on both the location along the spanwise direction and the wavelength. The time- and total surface-averaged Nusselt number for a wavy cylinder with $\lambda = \pi/2$ is larger than that for a smooth cylinder, whereas that with $\lambda = \pi/4$ and $\pi/3$ is smaller than that for a smooth cylinder. However, because the surface area exposed to heat transfer for a wavy cylinder is larger than that for a smooth cylinder, the total heat transfer rate for a wavy cylinder with different wavelengths of $\lambda = \pi/4, \pi/3$ and $\pi/2$ is larger than that for a smooth cylinder.

1. Introduction

The phenomenon of flow separation, bluff body wake and the prediction of heat transfer from a cylinder have been intensely studied for a long time because of their fundamental significance in flow physics and their practical importance in aerodynamic and heat transfer applications [1–14]. The generation and evolution of vortices in the wake region have a big effect on the drag, heat transfer, flow-induced vibration and noise problems. For these reasons, many methods have been proposed to control the dynamics of the wake vortices with the aim of reducing the fluctuating lift force and the magnitude of the mean drag force as well as to enhance the heat transfer. One approach to achieve this goal is to introduce some forms of three-dimensional (3D) geometric disturbance to the base form of a nominally two-dimensional (2D) bluff body.

Among the 3D geometric disturbances, the waviness of the cylinder having the sinusoidal variation in the cross sectional area along the spanwise direction has been considered to investigate its effect on the flow characteristics such as the wake vortices and the body forces. Ahmed and Bays-Muchmore [15] investigated experimentally the transverse flow over a wavy cylinder. They obtained the pressure distributions on the surfaces of several wavy cylinders for different axial wavelengths at a Reynolds number of 20,000 based on the mean diameter. They found that the sectional drag coefficient at the node was greater than that at the saddle and that the significant spanwise pressure gradients resulted in 3D flow separation. Lam et al. [16] investigated experimentally the effects of the surface waviness of cylinders on the mean drag and the fluctuating lift. They found that the mean drag coefficients and fluctuating lift coefficients of wavy cylinders were lower than those of the smooth cylinder in the range of $Re = 20{,}000–50{,}000$. A drag reduction of up to 20% can be achieved depending on the degree of obliqueness $a^2/(\lambda D)$ of the wavy cylinder, where a and λ are the amplitude and the length of wave, respectively. They found that the Strouhal number in the range of $Re = 10{,}000–60{,}000$ was around 0.2, which was equal to the value of the smooth cylinder. Lam et al. [17] investigated the flow characteristics experimentally in the range of $Re = 3000–9000$. They concluded that the average vortex formation length to over half a wavelength of the wavy cylinder was longer than that of the smooth cylinder, resulting in drag reduction and suppression of the vortex-induced vibration. They observed that the spanwise flow moved from the saddle plane towards the nodal plane. They deduced that the shear layers shed from the points near the saddles extended along the spanwise direction, while the shear layers near the nodes contracted and accelerated. As a result, the wake showed the characteristics of incoherent turbulence due to enhanced turbulent mixing. Zhang et al. [18] investigated experimentally the 3D flow structures of

* Corresponding author. Tel.: +82 51 510 2440; fax: +82 51 512 9835.
E-mail address: myha@pusan.ac.kr (M.Y. Ha).

0017-9310/$ - see front matter © 2008 Elsevier Ltd. All rights reserved.
doi:10.1016/j.ijheatmasstransfer.2008.05.032

Nomenclature

a	normalized amplitude of the wave
c	space-averaged streamwise exit velocity
C_D	drag coefficient
C_L	lift coefficient
C_{Pb}	base suction pressure
d	normalized diameter
f	momentum forcing
h	heat source or sink
L	spanwise arc length of wavy surface
n	normal direction to the wall
Nu	local Nusselt number
$\overline{Nu}$	time-averaged local Nusselt number
$\langle Nu\rangle$	spanwise local surface-averaged Nusselt number
$\langle\overline{Nu}\rangle$	time- and spanwise local surface-averaged Nusselt number
$\langle\langle Nu\rangle\rangle$	total surface-averaged Nusselt number
$\langle\langle\overline{Nu}\rangle\rangle$	time- and total surface-averaged Nusselt number
P	pressure
Pr	Prandtl number
q	mass source/sink
Re	Reynolds number
r	normalized local radius
S	arc length
t	time
t_P	period of time integration
T	temperature
T_s	cylinder surface temperature
u, v, and w	velocity components in x, y and z directions
W	surface area of cylinder
x, y, z	Cartesian coordinates

Greek symbols

α	thermal diffusivity
λ	normalized wavelength
θ	angle of circular cylinder
ρ	density
υ	kinematic viscosity

Sub/superscripts

rms	root mean square
z	spanwise local value
∞	free-stream
$\overline{\ }$	time-averaged quantity
$\langle\rangle$	spanwise local surface-averaged quantity
$\langle\langle\rangle\rangle$	total surface-averaged quantity

the near-wake behind a wavy cylinder at $Re = 3000$. They concluded that the presence of the waviness modified the near-wake structure and the streamwise vortices significantly and contributed to the pronounced spanwise periodicity of the flow structure in the near-wake of the wavy cylinder. Lee and Nguyen [19] investigated experimentally the drag force, mean velocity and turbulence intensity profiles of the wake behind a wavy cylinder in the range of $Re = 5000$–$20{,}000$. They found that wavy cylinders reduced drag coefficient compared with the smooth cylinder and the wake structure varied periodically along the spanwise direction. They concluded that the vortex formation length for a wavy cylinder was longer than that of a smooth cylinder and the elongation of vortex formation length led to the drag reduction.

The above-mentioned studies elucidated some prominent flow features past a wavy cylinder. However, it is hard to find previous studies which have dealt with heat transfer around a wavy cylinder. Also the previous research for a wavy cylinder was mainly concentrated on the study for flow in the turbulence regime. Thus the purpose of the present study is to investigate numerically the three-dimensional flow and heat transfer characteristics around a wavy cylinder at a Reynolds number of 300 using both the finite volume method and the immersed boundary method. The present computational results around a wavy cylinder with different wavelengths are compared with those around a smooth cylinder, in order to see the effects of the presence of waviness along the spanwise direction on the fluid flow and heat transfer around a wavy cylinder.

2. Computational details

The immersed boundary method is used to simulate flow and thermal fields over a wavy cylinder. Therefore, the governing equations describing unsteady incompressible viscous flow and thermal fields in the present study are the momentum, continuity and energy equations:

$$\frac{\partial u_i}{\partial t}+\frac{\partial u_i u_j}{\partial x_j}=-\frac{\partial P}{\partial x_i}+\frac{1}{Re}\frac{\partial^2 u_i}{\partial x_j \partial x_j}+f \tag{1}$$

$$\frac{\partial u_i}{\partial x_i}-q=0 \tag{2}$$

$$\frac{\partial T}{\partial t}+\frac{\partial u_j T}{\partial x_j}=\frac{1}{RePr}\frac{\partial^2 T}{\partial x_j^2}+h \tag{3}$$

where x_i are Cartesian coordinates, u_i are the corresponding velocity components, t is the time, P is the pressure, and T is the temperature. The momentum forcing f and mass source/sink q are applied on the body surface or inside the body to satisfy the no-slip and mass conservation on the cell containing the immersed boundary. In Eq. (3), the heat source/sink h is applied to satisfy the iso-thermal boundary condition on the immersed boundary. All the variables are non-dimensionalized by the cylinder mean diameter corresponding to the smooth cylinder diameter d, free-stream velocity U_∞ and the cylinder surface temperature T_S. The above non-dimensionalization results in two dimensionless parameters: $Re = U_\infty d/\upsilon$ and $Pr = \upsilon/\alpha$ where υ and α are the kinematic viscosity and thermal diffusivity. In the simulations to be reported here the Prandtl number, Pr, is a constant 0.71 corresponding to air. The Reynolds number of $Re = 300$ is considered.

A two-step time-split scheme is used to advance the flow field. This scheme is based on the previous works of Kim and Moin [20] and Zang et al. [21]. First the velocity is advanced from time level 'n' to an intermediate level '$*$' by solving the advection–diffusion equation without the pressure term. In the advection–diffusion step, the non-linear terms are treated explicitly using the third-order Adams–Bashforth scheme. The diffusion terms are treated implicitly using the Crank–Nicolson scheme. Then the Poisson equation for pressure, which is derived by using mass conservation, is solved fully implicitly. Once the pressure is obtained, the final divergence-free velocity field at '$n+1$' is obtained with a pressure-correction step. The temperature field is advanced in a similar manner with the third-order Adams–Bashforth scheme for the advection term and the Crank–Nicolson scheme for the diffusion term. The central difference scheme with second-order accuracy based on the finite volume method is used for the spatial discretization. Additionally, a second-order linear, bilinear or trilinear interpolation scheme is applied to satisfy the no-slip and iso-thermal conditions on the immersed boundary. Further details

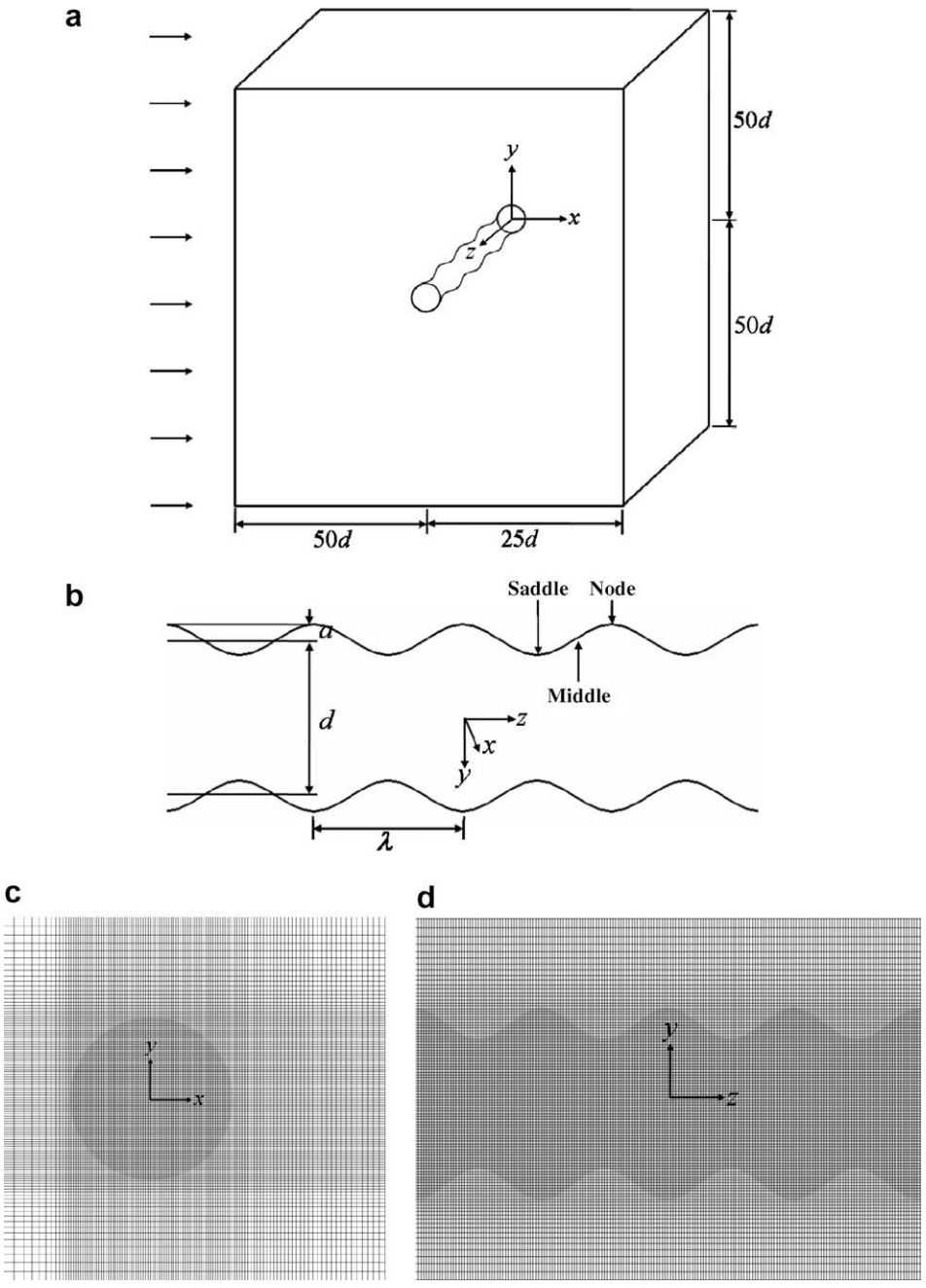

Fig. 1. (a) Computational domain and coordinate system, (b) geometry of the wavy cylinder and grid system in (c) x–y plane and (d) y–z plane near the wavy surface.

of the immersed-boundary method are given in Kim et al. [22] and Kim and Choi [23].

The computational domain and coordinate system are shown in Fig. 1(a). The size of computational domain is $-50 \leqslant x \leqslant 25$ and $-50 \leqslant y \leqslant 50$ for the streamwise and transverse directions, respectively. The spanwise domain (L_z) has different sizes for four different cases as shown in Table 1. The grid points in the x and y directions are uniformly distributed within the cylinder while a hyperbolic tangent distribution is in the outer region, and uniform grids are used in the spanwise direction. At the inflow and far-field boundaries, the Dirichlet boundary conditions, $u = 1$, $v = 0$, $w = 0$ and $T = 0$, are enforced. On the surface of the cylinder or immersed boundary, no-slip and no-penetration boundary conditions, $u = 0$, $v = 0$ and $w = 0$, are imposed for the velocity field, while an isothermal boundary condition, $T = 1$, is enforced for the temperature. The convective boundary conditions, $\partial u_i/\partial t + c\partial u_i/\partial x = 0$ and, $\partial T/\partial t + c\partial T/\partial\, x = 0$ are applied at the outflow boundary, where c is the space-averaged streamwise exit velocity, u, v and w are the velocity components in x, y and z directions, respectively. A periodic boundary condition is used in the spanwise direction.

Table 1
Grid and geometrical parameters used

	λ	$N_x \times N_y \times N_z$	L_z	a
Wavy cylinder	$\pi/4$	$260 \times 220 \times 186$	π	0.1
	$\pi/3$	$260 \times 220 \times 186$	$4\pi/3$	0.1
	$\pi/2$	$260 \times 220 \times 186$	2π	0.1
Smooth cylinder	–	$260 \times 220 \times 49$	π	0.0

The geometry of the wavy cylinder is described by $d_z = d + 2a\cos(2\pi z/\lambda)$. Here, d_z is the normalized local diameter, d is the normalized diameter, a is the normalized amplitude of the surface

curve, λ is the normalized wavelength, and z is the spanwise location. The terminology used to describe the wavy cylinder is defined in Fig. 1(b). The axial locations of the maximum diameter are hereafter termed 'node', while the axial locations of the minimum diameter are denoted as 'saddle'. The origin of the coordinate is located at the center of a nodal cross-section.

The number of grid points used in the present calculation is given in Table 1. The grid independence study to find optimum grid resolution has been performed for the wavy cylinder with a wavelength value of $\pi/2$ and the smooth cylinder. For the wavy cylinder, the grid dimensions of the coarse, medium and fine grid systems considered are $200 \times 180 \times 146$, $260 \times 220 \times 186$ and $300 \times 250 \times 209$ in the x, y and z directions, respectively. In case of the smooth cylinder, the grid dimensions of the coarse, medium and fine grid systems considered are $200 \times 180 \times 36$, $260 \times 220 \times 49$ and $300 \times 250 \times 64$ in the x, y and z directions, respectively. For both the wavy and the smooth cylinders, the difference in time-averaged body forces and Nusselt numbers obtained using the medium and fine grid systems is less than 0.05%. However, these values using the coarse grid system show a little deviation from those using the medium and fine grid systems. Accordingly, we used respectively the medium grid system of $260 \times 220 \times 186$ and $260 \times 220 \times 49$ for the wavy cylinder and the smooth cylinder in the present computation. The condition of CFL $\leqslant$0.3 is chosen to determine the non-dimensional time step used in the present calculation. A series of computational studies have been carried out for the fixed value of $a = 0.1$ and the different wavelength values of $\pi/4$,$\pi/3$ and $\pi/2$.

Once the velocity and temperature fields are obtained, the local, time-averaged local, spanwise local surface-averaged-, time- and spanwise local surface-averaged-, total surface-averaged, and time- and total surface-averaged Nusselt number are defined as

$$\begin{aligned} Nu &= \tfrac{\partial T}{\partial n}\big|_{\text{wall}} & \overline{Nu} &= \tfrac{1}{t_P}\int_0^{t_P} Nu\,\mathrm{d}t \\ \langle Nu\rangle &= \tfrac{1}{W_z}\int_0^{W_z} Nu\,\mathrm{d}S & \langle\overline{Nu}\rangle &= \tfrac{1}{t_P}\int_0^{t_P}\langle Nu\rangle\,\mathrm{d}t \\ \langle\langle Nu\rangle\rangle &= \tfrac{1}{L}\int_0^{L}\langle Nu\rangle\,\mathrm{d}z & \langle\langle\overline{Nu}\rangle\rangle &= \tfrac{1}{t_P}\int_0^{t_P}\langle\langle Nu\rangle\rangle\,\mathrm{d}t \end{aligned} \tag{4}$$

where n is the normal direction to the walls, W_z is the spanwise local surface area, L is the spanwise arc length and t_P is the period of time integration.

The validation of the present numerical method has been performed by the comparisons with previous experimental and computational results for a smooth cylinder at $Re = 300$ as shown in Table 2. Drag, lift and base suction coefficients are in good agreement with those of Kim and Choi [24], Kravchenko et al. [25] and Posdziech and Grundmann [26]. Also, the present Nusselt number represents the results of Churchill and Bernstein [27] well.

3. Results and discussion

The temperature fields around a wavy cylinder depend on the flow fields because the temperature is a passive scalar which is governed by the distribution of fluid flow. The presence of waviness along the spanwise direction increases the three-dimensionality in the fluid flow past a wavy cylinder compared with the flow around a smooth cylinder. Fig. 2 shows the contours of the instantaneous spanwise velocity in the $x-z$ plane at $y = 0$ and 0.4 for the smooth cylinder and the wavy cylinder with $\lambda = \pi/2$. Although the shape of the smooth cylinder is two-dimensional, it is well known that the three-dimensional transition in the wake of the smooth cylinder occurs near $Re = 194$, as shown by Williamson [8]. Thus, at $Re = 300$ considered in the present study, the spanwise velocity for a smooth cylinder shows clearly three-dimensional characteristics in the wake region at two different positions of $y = 0$ and 0.4, as shown in Fig. 2(a) and (b). For the case of the wavy cylinder, the sign of the spanwise velocity in front of wavy cylinder varies regularly along the spanwise direction as shown in Fig. 2(c) and (d), depending on the shape of the wave, which does not appear in the front region of the smooth cylinder. At the more distant position of $y = 0.4$ from the vertical center of cylinder ($y = 0$), the strength of three-dimensionality of the flow in front of wavy cylinder becomes weaker owing to the reduction of waviness and the direction of spanwise velocity in the near wake region become more regular, compared with those at $y = 0$, as shown in Fig. 2(c) and (d).

Fig. 3 shows the time-averaged flow and temperature fields in $y-z$ plane for different streamwise locations for the wavy cylinder with $\lambda = \pi/2$. For the case of the smooth cylinder, the spanwise component of velocity does not exist in the time-averaged flow field because the shape of the smooth cylinder is homogeneous in the spanwise direction. In contrast, for the case of the wavy cylinder, the spanwise velocity appears because the flow follows the wavy surface. As a result, in front of the wavy cylinder at $x = -0.5$, the spanwise flow moves from the node to the saddle alternately as shown in Fig. 3(a). As the flow moves downward, the direction of spanwise flow is opposite to that of the spanwise flow in front of the wavy cylinder, resulting in the flow moving from the saddle toward the node, as shown in Fig. 3(b) and (c). The isotherms in the upward regions of $x = -0.5$ and 0 are distributed densely near the surface of wavy cyl-

Table 2
Comparisons between the present study with previous results

	$\overline{C_D}$	$C_{L,rms}$	$\overline{C_{Pb}}$	$\langle\langle\overline{Nu}\rangle\rangle$
Present	1.30	0.46	−1.01	8.87
Kim and Choi [24]	1.32	0.46	−1.03	–
Kravchenko et al. [25]	1.28	0.40	−1.01	–
Posdziech and Grundmann [26]	1.27	0.44	−1.00	–
Churchill and Bernstein [27]	–	–	–	8.71

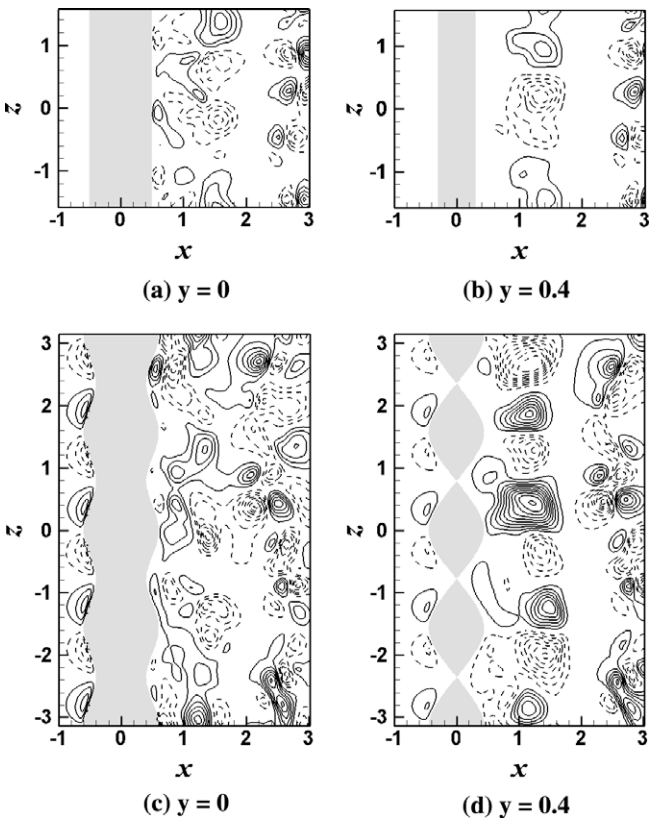

Fig. 2. Contours of instantaneous spanwise velocity in the two different x–z planes for the smooth cylinder (a and b) and the wavy cylinder with $\lambda = \pi/2$ (c and d) (Contour values range from −0.5 to 0.5 with 21 levels).

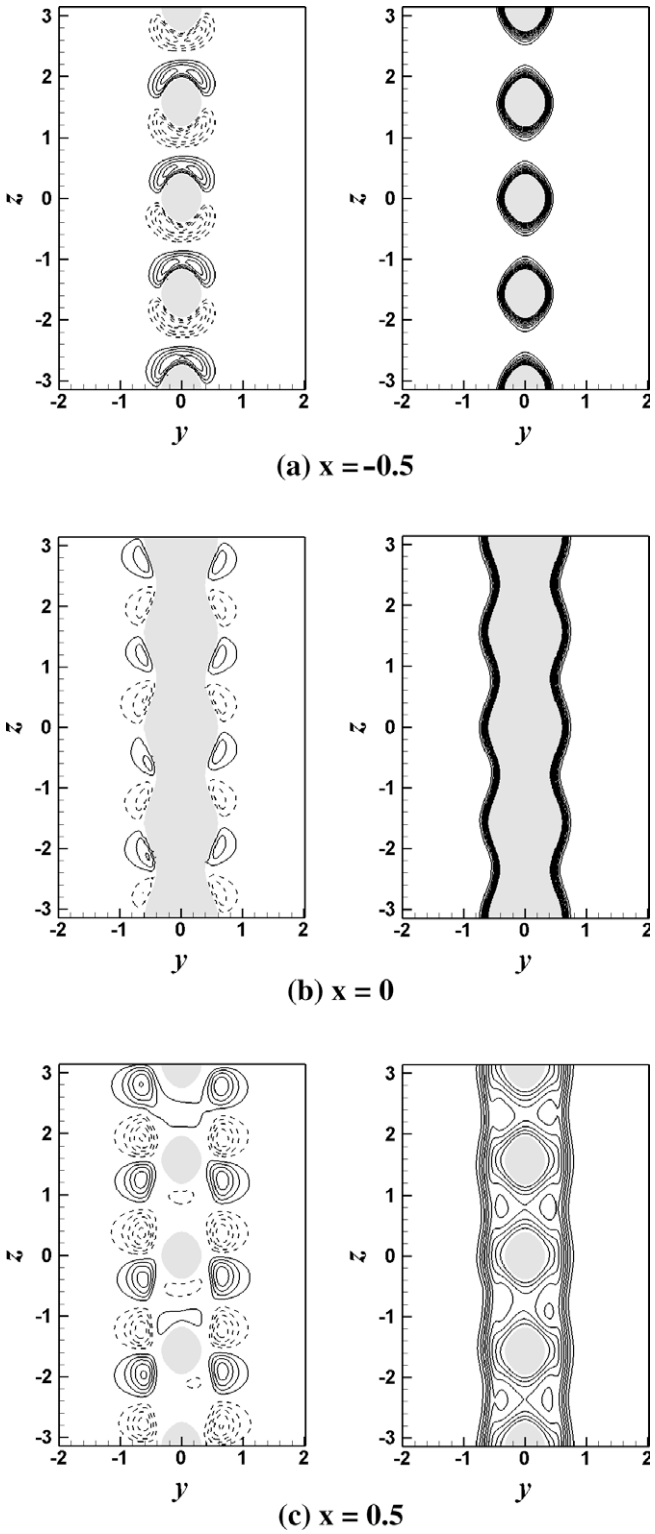

Fig. 3. Contours of the time-averaged spanwise velocity (left column) and temperature (right column) for the wavy cylinder with $\lambda = \pi/2$ (Contour values of spanwise velocity range from −0.3 to 0.3 with 25 levels and contour values of temperature range from 0.1 to 0.9 with 9 levels).

inder as shown in Fig. 3(a) and (b), whereas the isotherms in the downward region of $x = 0.5$ are distributed widely due to flow mixing as shown in Fig. 3(c).

In order to observe clearly the occurrence of the spanwise flow induced by the presence of waviness along the spanwise direction shown in Fig. 3, the streamlines around a wavy cylinder are compared with those around a smooth cylinder, as shown in Fig. 4. The streamlines in Fig. 4 are shown in the x–z plane slightly over the cylinder. The flow in front of the wavy cylinder converges on the saddle, whereas the flow in the rear of the wavy cylinder diverges from the saddle, which is not observed for the case of the smooth cylinder. These results are consistent with the previous observations by Lam et al. [17].

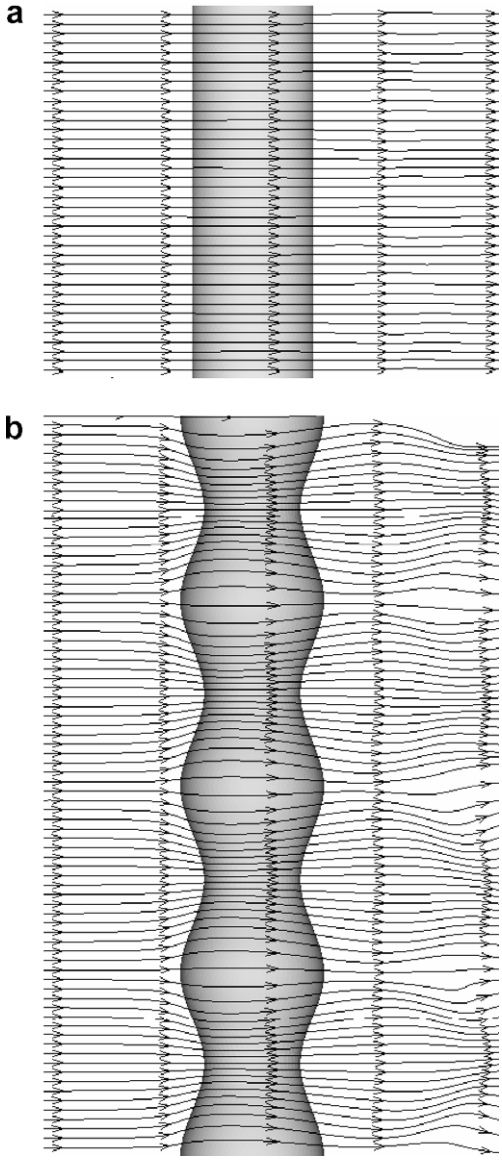

Fig. 4. Streamlines around (a) smooth cylinder and (b) wavy cylinder with $\lambda = \pi/2$.

For the purpose to investigate the effect of the presence of waviness along the spanwise direction on the upstream flow in front of the cylinder, the time-averaged streamwise velocity $\bar{u}$ and pressure $\overline{P}$ along the spanwise distance for the smooth cylinder and three different wavy cylinders with $\lambda = \pi/4, \pi/3$ and $\pi/2$ at the position of $x = -0.7$ and $y = 0$ are shown in Fig. 5. The time-averaged streamwise velocity and pressure for the case of a smooth cylinder has constant values, meaning that $\bar{u}$ and $\overline{P}$ have no variation along the spanwise direction in front of the smooth cylinder. However, for the case of a wavy cylinder, $\bar{u}$ and $\overline{P}$ vary as a function of distance in the spanwise direction in front of the wavy cylinder. The distribution of $\bar{u}$ and $\overline{P}$ for three different wavy cylinders is generally similar with a parabolic shape. The value of the radius at the node of the wavy cylinder is highest whereas the value of the radius at the saddle is lowest. Thus the pressure has a maximum

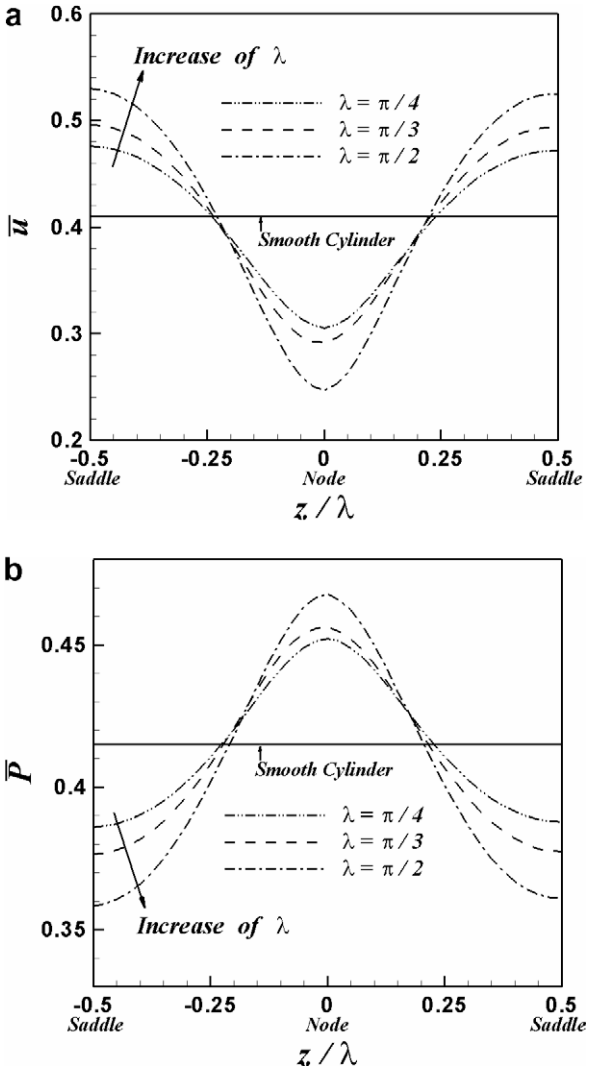

Fig. 5. Time-averaged streamwise velocity and pressure along the spanwise distance for the smooth cylinder and three different wavy cylinders with $\lambda = \pi/4$, $\pi/3$ and $\pi/2$ at the position of $x = -0.7$ and $y = 0$.

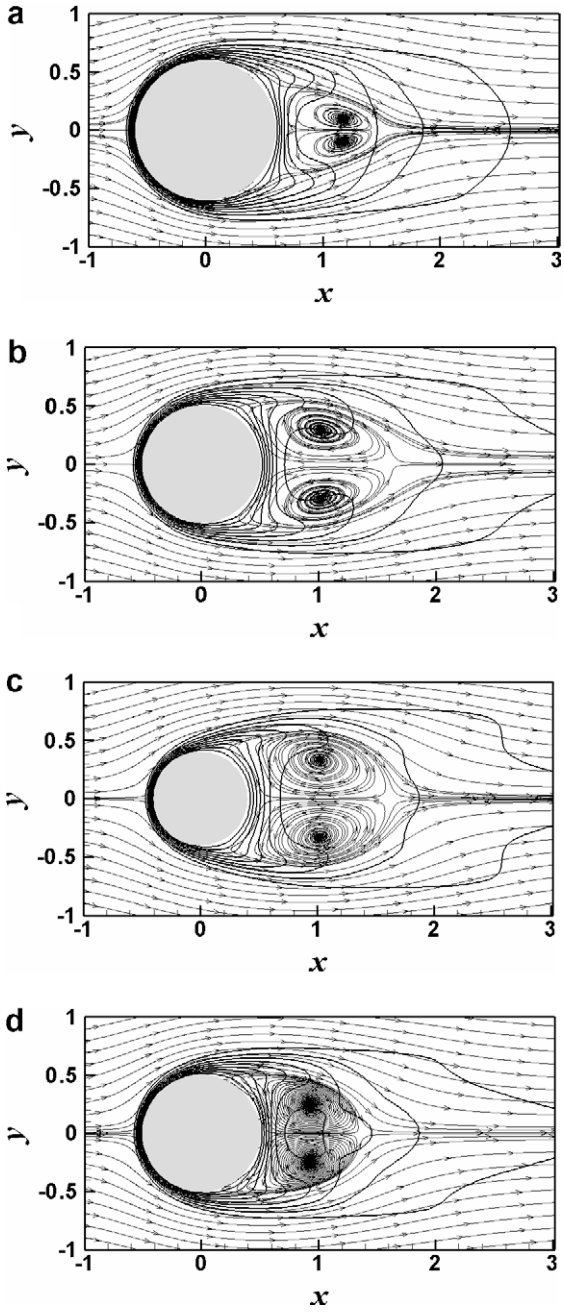

Fig. 6. Time-averaged streamlines and superimposed temperature contours at three different spanwise locations for $\lambda = \pi/2$; (a) node, (b) middle and (c) saddle and (d) smooth cylinder (Contour values of temperature range from 0.1 to 0.9 with nine levels).

value at the node and a minimum one at the saddle, whereas the velocity has a minimum value at the node and a maximum one at the saddle. However, the magnitude of $\bar{u}$ and $\overline{P}$ for the wavy cylinders depends on the wavelength. As the wavelength increases, the extent of variation in $\bar{u}$ and $\overline{P}$ becomes wider. As a result, the values of $\bar{u}$ at the node for $\lambda = \pi/2$ is smaller than that for $\lambda = \pi/3$ and $\pi/4$, whereas $\bar{u}$ at the saddle for $\lambda = \pi/2$ is larger than that for $\lambda = \pi/3$ and $\pi/4$. The variation in the magnitude of $\overline{P}$ is opposite to $\bar{u}$ as shown in Fig. 5.

Fig. 6 shows time-averaged streamlines and superimposed isotherms at different spanwise locations of the node, middle and saddle of a wavy cylinder when $\lambda = \pi/2$. Because the flow on the node plane converges in the near wake as shown in Fig. 4, a pair of vortices on the node side is squeezed in both the longitudinal and transverse direction as shown in Fig. 6(a). As a result, the separation is delayed and the separation point moves to the streamwise direction. As we move from the node to the saddle, the flow spreads out more because the flow diverges from the node to the saddle. As a result the separation point moves to the upstream direction and the size of the recirculation bubble in the near wake becomes larger. The distribution of isotherms around a wavy cylinder depends on this flow pattern strongly. At the front stagnation point, the thermal gradient has a maximum value with the smallest thermal boundary layer thickness. As the flow moves to the downstream direction from the stagnation point along the wavy cylinder surface, the thermal gradient decreases with increasing thermal boundary layer thickness. The thermal gradient has a minimum value with the largest thermal boundary layer thickness at the separation point. As the flow moves further to the downstream direction from the separation point along the wavy cylinder surface, the thermal gradient increases again with decreasing thermal boundary layer thickness. Because the flow pattern around a wavy cylinder varies along the spanwise direction, the distribution of isotherms also varies along the spanwise direction as shown in Fig. 6.

Fig. 7 shows the total surface-averaged Nusselt number as a function of time for a smooth cylinder and wavy cylinders with

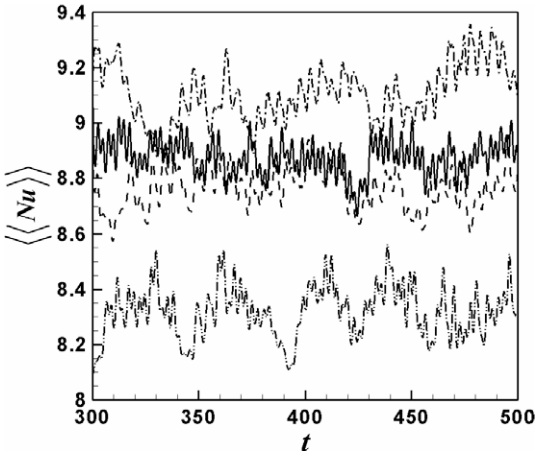

Fig. 7. Total surface-averaged Nusselt number as a function of time: -···-, $\lambda = \pi/4$; - - -, $\lambda = \pi/3$; —·—, $\lambda = \pi/2$ and —, smooth cylinder.

different wavelengths of $\lambda = \pi/4,\pi/3$ and $\pi/2$. The total surface-averaged Nusselt number for the smooth cylinder and wavy cylinders shows strong time-dependence characteristics. The total surface-averaged Nusselt numbers have different time-averaged mean values depending on the wavelength, because the flow and temperature fields have different distributions depending on the wave pattern of wavy cylinder.

Fig. 8 shows the time-averaged local Nusselt number $\overline{Nu}$, temperature $\overline{T}$ and streamwise velocity $\bar{u}$ as a function of the circumferential direction θ at different spanwise locations of node, middle and saddle for different wavelengths of $\lambda = \pi/4,\pi/3$ and $\pi/2$. The distribution of $\overline{Nu}, \overline{T}$ and $\bar{u}$ at different spanwise locations for the wavy cylinders is compared with those for the smooth cylinder. $\theta = 0°$ and 180° in Fig. 8 represent the front and rear stagnation points. For both the smooth cylinder and the wavy cylinder, the distribution of $\overline{Nu}$ as a function of θ shows a similar pattern. $\overline{Nu}$ has a maximum value at the front stagnation point of $\theta = 0°$. When θ increases from the front stagnation point to the separation point, $\overline{Nu}$ decreases and reaches a minimum value at the separation point (see Table 3 for the separation points for the wavy and smooth cylinders). If we increases θ further from the separation point to the rear stagnation point, $\overline{Nu}$ increases again due to the mixing effect caused by the flow separation.

However, the magnitude of time-averaged local Nusselt number for a wavy cylinder depends on the wavelength of wavy cylinder. Because the diameter at the node of the wavy cylinder is larger than at the middle and saddle of the wavy cylinder and the smooth cylinder, the approaching cold fluid meets the node of wavy cylinder first. As a result, the values of $\overline{Nu}$ and $\bar{u}$ at the node of wavy cylinder are generally larger than those at the middle and saddle of the wavy cylinder, whereas $\overline{T}$ at the node is generally smaller than that at the middle and saddle, except for the wake region. If the wavelength is small, the slope of the valley formed on the wavy cylinder becomes sharper, giving more resistance to the flow around a wavy cylinder. As a result, for the case of $\lambda = \pi/4$, we can observe big differences in the magnitude of $\overline{Nu}, \overline{T}$ and $\bar{u}$ for different spanwise positions of the node, middle and saddle of the wavy cylinder and for the smooth cylinder. However, if we increase the wavelength, the slope of the valley formed on the wavy cylinder becomes gentle and the resistance to the flow around the wavy cylinder decreases, resulting in the decreasing differences in the magnitude of $\overline{Nu}, \overline{T}$ and $\bar{u}$ at different positions of the node, middle and saddle of the wavy cylinder. For the case of $\lambda = \pi/2$, the streamwise velocity in the front of cylinder becomes larger with increasing wavelength and more cold fluid is transferred to the saddle directly. As a result $\overline{Nu}$ near the front stagnation has the largest value at the saddle.

Fig. 9 shows the isometric views for the distribution of time-averaged local Nusselt numbers ($\overline{Nu}$) over the surfaces for the smooth cylinder and the wavy cylinders with different wavelengths of $\lambda = \pi/4,\pi/3$ and $\pi/2$. S in Fig. 9 is the arc length defined by $r_z \cdot \theta$ where r_z is the local radius along the spanwise direction and $0 \leqslant \theta \leqslant \pi$. In Fig. 9(b)–(d), the spanwise distance z is normalized by the wavelength λ of the corresponding wavy cylinder. As expected, $\overline{Nu}$ for the smooth cylinder is independent of the spanwise direction and has a maximum value at the front stagnation point and a minimum one at the separation point, as shown in Fig. 9(a). For the cases of the wavy cylinders, the variation of $\overline{Nu}$ along the circumferential direction is similar to that for a smooth cylinder with a maximum value at the front stagnation point and a minimum value at the separation point. However, as we have already discussed, the variation of $\overline{Nu}$ along the circumferential direction for the wavy cylinder shows a strong dependence on the spanwise direction. Generally, the value of $\overline{Nu}$ for a wavy cylinder has a peak value at the node and decreases in the form of a parabolic shape as we move from the node to the saddle, as shown in Fig. 9(b)–(d).

Fig. 10 shows the time- and spanwise local surface-averaged Nusselt number, $\langle\overline{Nu}\rangle$, as a function of z/λ for the wavy cylinders with different wavelengths of $\lambda = \pi/4$, $\pi/3$ and $\pi/2$ and the smooth cylinder. $\langle\overline{Nu}\rangle$ for a smooth cylinder has a constant value, meaning that $\langle\overline{Nu}\rangle$ does not depend on the spanwise direction. However, $\langle\overline{Nu}\rangle$ for wavy cylinders has a maximum value at the node and decreases as we move from the node to the saddle, which is similar to the distribution of time-averaged local Nusselt number shown in Fig. 8. The values of $\langle\overline{Nu}\rangle$ at the node for the wavy cylinders are larger than $\langle\overline{Nu}\rangle$ for the smooth cylinder, with the largest value when $\lambda = \pi/4$. For the cases of $\lambda = \pi/3$ and $\pi/2$, the values of $\langle\overline{Nu}\rangle$ in the large part of the spanwise direction for the wavy cylinder are lower than those for the smooth cylinder. When $\lambda = \pi/4, \langle\overline{Nu}\rangle$ at the saddle is the lowest value. When $\lambda = \pi/2, \langle\overline{Nu}\rangle$ approaches the value of a smooth cylinder as we move from the node to the saddle.

Table 4 shows the time-averaged drag coefficient $\overline{C_D}$, time- and total surface-averaged Nusselt number $\langle\langle\overline{Nu}\rangle\rangle$ and time- and spanwise local surface-averaged Nusselt number $\langle\overline{Nu}\rangle$ for the smooth cylinder and the wavy cylinders with different wavelengths of $\lambda = \pi/4,\pi/3$ and $\pi/2$. For the case of the wavy cylinders, because the diameter at the node is largest, the incoming flow hits first the node and as a result $\langle\overline{Nu}\rangle$ has the largest values at the node. As we move from the node to the saddle, $\langle\overline{Nu}\rangle$ decreases with decreasing diameter, showing the dependence of $\langle\overline{Nu}\rangle$ on the spanwise direction. However, for the case of the smooth cylinder, $\langle\overline{Nu}\rangle$ does not vary along the spanwise direction and has a constant value. The values of $\langle\overline{Nu}\rangle$ at the node for the wavy cylinders with $\lambda = \pi/4,\pi/3$ and $\pi/2$ are respectively 33%, 18% and 8.7% larger than those of the a smooth cylinder. The values of $\langle\overline{Nu}\rangle$ at the saddle for wavy cylinders with $\lambda = \pi/4,\pi/3$ and $\pi/2$ are, respectively, 25%, 11% and 0.1% lower than those of the smooth cylinder. The values of the time-averaged drag coefficient $\overline{C_D}$ for $\lambda = \pi/2$ and $\pi/3$ are about 6.15% and 1.54% lower than those of the smooth cylinder, respectively, whereas the value of $\overline{C_D}$ for $\lambda = \pi/4$ is about 3.85% higher than that of the smooth cylinder. The value of time- and total surface-averaged Nusselt number $\langle\langle\overline{Nu}\rangle\rangle$ for $\lambda = \pi/2$ is about 2.7% larger than that of the smooth cylinder whereas the values of $\langle\langle\overline{Nu}\rangle\rangle$ for $\lambda = \pi/4$ and $\pi/3$ are 1.2% and 6.2% less than that of the smooth cylinder, respectively, due to the before-mentioned reasons in Figs. 8 and 10. However, the total surface areas exposed for heat transfer for the cases of the wavy cylinders with $\lambda = \pi/4,\pi/3$ and $\pi/2$ are

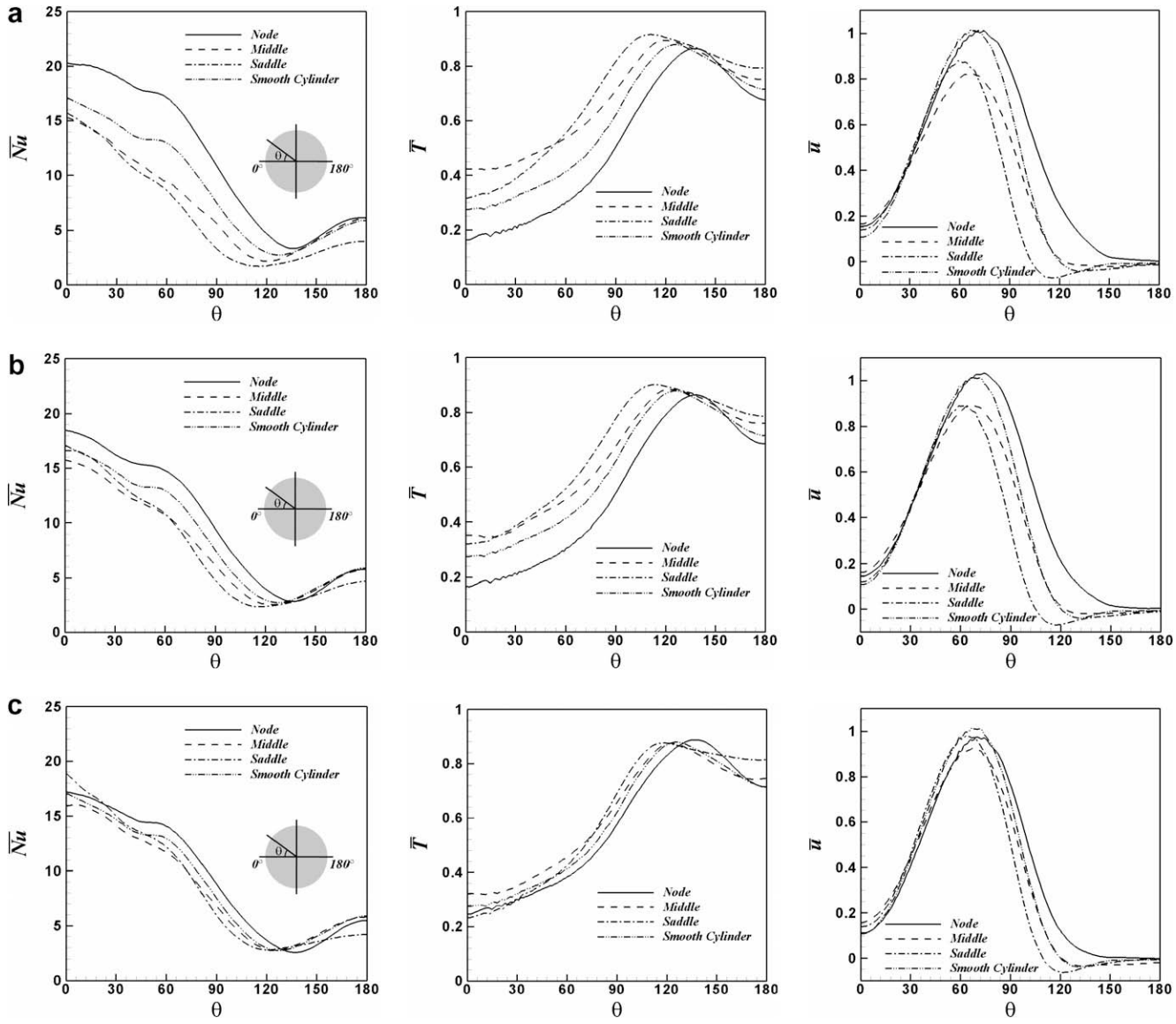

Fig. 8. Time-averaged local Nusselt number, temperature and streamwise velocity as a function of the circumferential direction θ at different spanwise locations for (a) $\lambda = \pi/4$, (b) $\lambda = \pi/3$ and (c) $\lambda = \pi/2$.

Table 3
Separation point for a smooth cylinder and wavy cylinders with different wavelengths of $\lambda = \pi/4$, $\pi/3$ and $\pi/2$

	λ	Node	Middle	Saddle
Wavy cylinder	$\pi/4$	136 º	121 º	115 º
	$\pi/3$	137 º	123 º	117 º
	$\pi/2$	137 º	126 º	121 º
Smooth cylinder	–	128 º		

about 15%, 9% and 4% larger than that for the smooth cylinder, respectively, due to the presence of waviness along the spanwise direction. As a result the total heat transfer rate for the cases of the wavy cylinders with $\lambda = \pi/4$, $\pi/3$ and $\pi/2$ are about 8%, 8% and 7% larger than that for the smooth cylinder, respectively, even though the values of $\langle\langle \overline{Nu} \rangle\rangle$ for the wavy cylinders with $\lambda = \pi/4$ and $\pi/3$ are lower than those for the smooth cylinder. Thus the wavy cylinder can be used as a method to enhance the heat transfer rate under the condition of lower flow resistance at the Reynolds number of 300.

4. Conclusions

The present study solves the three-dimensional and time-dependent equations to govern the fluid flow and heat transfer around wavy cylinders numerically using the finite volume method. The immersed boundary method is used to handle the geometry of a wavy cylinder in the rectangular grid system. In order to consider the effects of the presence of waviness along the spanwise direction on the fluid flow and heat transfer around a wavy cylinder, we adopted three different wavelengths of $\lambda = \pi/2$, $\pi/3$ and $\pi/4$ with the fixed wavy amplitude of 0.1 at a Reynolds number of 300 and a Prandtl number of 0.71, and compared the present results for the wavy cylinders with those for a smooth cylinder. The number of grid points used is more than 10 million. The present results for the smooth cylinder agree well with the previous research results, showing the validity of the present computation.

The occurrence of the spanwise flow, which is induced by the presence of waviness along the spanwise direction of the wavy cylinders, is observed by comparing the streamlines and spanwise velocity contours around the smooth cylinder with those

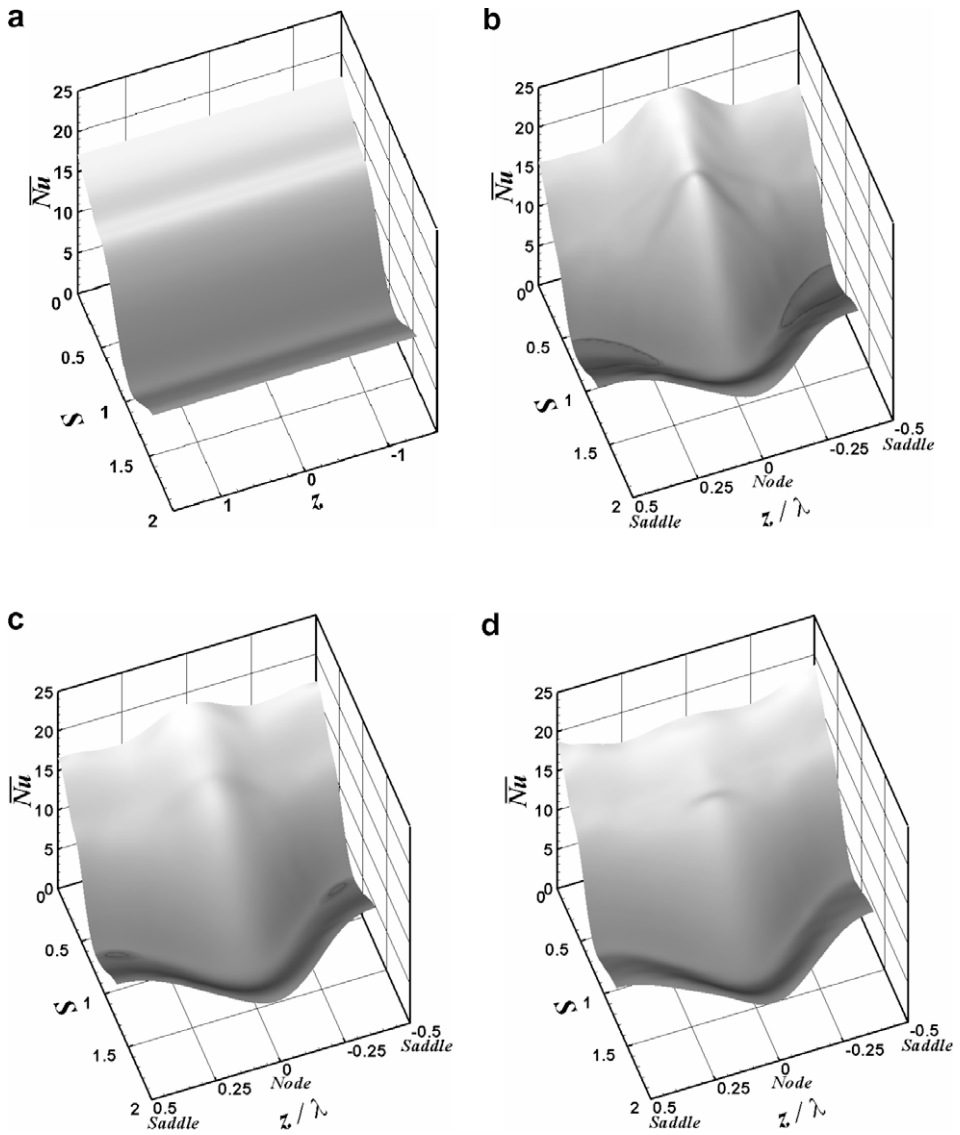

Fig. 9. Isometric views for the distribution of time-averaged local Nusselt number over the surfaces for (a) the smooth cylinder and the wavy cylinders with different wavelengths of (b)$\lambda = \pi/4$, (b) $\lambda = \pi/3$ and (c) $\lambda = \pi/2$.

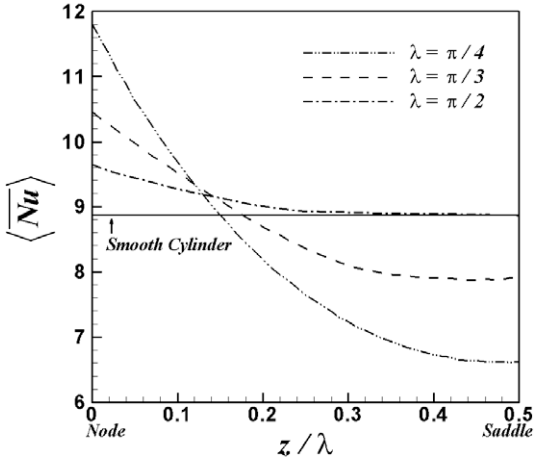

Fig. 10. Time- and spanwise local surface-averaged Nusselt number as a function of z/λ for the smooth cylinder and the wavy cylinders with different wavelengths of $\lambda = \pi/4, \pi/3$ and $\pi/2$.

Table 4
Time-averaged drag coefficient, time- and total surface-averaged Nusselt number and time- and spanwise local surface-averaged Nusselt number for a smooth cylinder and wavy cylinders with different wavelengths of $\lambda = \pi/4$, $\pi/3$ and $\pi/2$

	λ	$\overline{C_D}$	$\langle\langle\overline{Nu}\rangle\rangle$	$\langle\overline{Nu}\rangle$		
				Node	Middle	Saddle
Wavy cylinder	$\pi/4$	1.35	8.32	11.79	7.65	6.62
	$\pi/3$	1.28	8.76	10.46	8.36	7.89
	$\pi/2$	1.22	9.11	9.64	8.92	8.86
Smooth cylinder	–	1.30	8.87	–	–	–

around the wavy cylinders. The flow converges on the saddle in front of the wavy cylinder and diverges from the saddle in the back of the wavy cylinder. As we move from the node to the saddle of the wavy cylinder, the separation along the circumferential direction on the wavy cylinder surface occurs earlier and the size of a pair of time-averaged vortices formed in this direction becomes larger.

The variation of the time-averaged local Nusselt numbers $\overline{Nu}$ along the circumferential direction for the wavy cylinders has a similar pattern to that of the smooth cylinder, having maximum and minimum values at the front stagnation and separation points, respectively. However, the variation of $\overline{Nu}$ for a wavy cylinder along the spanwise direction has a strong dependence on the location in the spanwise direction, with a larger value at the node than at the saddle of the wavy cylinder.

A value of time- and total surface-averaged Nusselt numbers $\langle\langle\overline{Nu}\rangle\rangle$ for $\lambda = \pi/2$ is higher than that of the smooth cylinder, whereas the values of $\langle\langle\overline{Nu}\rangle\rangle$ for $\lambda = \pi/4$ and $\pi/3$ are lower than that of the smooth cylinder. However the total heat transfer rate for the wavy cylinders is larger than that of the smooth cylinder because of the increase in the total surface area exposed to heat transfer. Thus the wavy cylinder can be used as a method to enhance the heat transfer rate under the condition of lower flow resistance at the Reynolds number of 300.

Acknowledgements

This work was supported by the Korea Foundation for International Cooperation of Science & Technology(KICOS) through a grant provided by the Korean Ministry of Education, Science & Technology (MEST) in 2007 (No. K20702000013-07E0200-01310). Prof. Yoon thanks the Advanced Ship Engineering Research Center (ASERC) of Pusan National University for the financial support through the Korea Science and Engineering Foundation.

References

[1] R.A. Ahmad, Steady-state numerical solution of the Navier–Stokes and energy equations around a horizontal cylinder at moderate Reynolds numbers from 100 to 500, Heat Transf. Eng. 17 (1996) 31–80.
[2] M. Braza, P. Chassaing, H.H. Minh, Numerical study and physical analysis of the pressure and velocity fields in the near wake of a circular cylinder, J. Fluid Mech. 165 (1986) 79–130.
[3] R. Mittal, S. Balachandar, Direct numerical simulation of flow past elliptic cylinders, J. Comput. Phys. 124 (1994) 351–367.
[4] H.S. Yoon, H.H. Chun, M.Y. Ha, H.G. Lee, A numerical study on the fluid flow and heat transfer around a circular cylinder in an aligned magnetic field, Int. J. Heat Mass Transf. 47 (2004) 4075–4085.
[5] H.S. Yoon, J.B. Lee, H.H. Chun, A numerical study on the fluid flow and heat transfer around a circular cylinder near a moving wall, Int. J. Heat Mass Transf. 50 (2007) 3507–3520.
[6] D. Lee, M. Ha, S. Balachandar, S. Lee, Numerical simulations of flow and heat transfer past a circular cylinder with a periodic array of fins, Phys. Fluids 16 (2004) 1273–1286.
[7] C.H.K. Williamson, Oblique and parallel modes of vortex shedding in the wake of a circular cylinder at low Reynolds numbers, J. Fluid Mech. 206 (1989) 579–628.
[8] C.H.K. Williamson, Vortex dynamics in the cylinder wake, Ann. Rev. Fluid Mech. (1996) 477–539.
[9] C.H.K. Williamson, Three-dimensional wake transition, J. Fluid Mech. 328 (1996) 345–407.
[10] K. Noto, K. Fujimoto, Formulation and numerical methodology for three-dimensional wake of heated circular cylinder, Numer. Heat Transf. A 49 (2006) 129–158.
[11] S.K. Wang, T.C. Hung, G.W. Lin, B.S. Pei, Numerical simulations for the phenomena of vortex-induced vibration and heat transfer of a circular cylinder, Numer. Heat Transf. A 45 (2004) 719–736.
[12] S. Singh, G. Biswas, A. Mukhopadhyay, Effect of thermal buoyancy on the flow through a vertical channel with a built-in circular cylinder, Numer. Heat Transf. A 34 (1998) 769–789.
[13] M.S. Phanikumar, R.L. Mahajan, Numerical analysis of unsteady thermosolutal convection over a horizontal isothermal circular cylinder, Numer. Heat Transf. A 33 (1998) 673–700.
[14] R. Bradean, D.B. Ingham, P.J. Heggs, I. Pop, Unsteady free convection adjacent to an impulsively heated horizontal circular cylinder in porous media, Numer. Heat Transf. A 32 (1997) 325–346.
[15] A. Ahmed, B. Bays-Muchmore, Transverse flow over a wavy cylinder, Phys. Fluids A4 (1992) 1959–1967.
[16] K. Lam, F.H. Wang, J.Y. Li, R.M.C. So, Experimental investigation of the mean and fluctuating forces of wavy (varicose) cylinders in a cross-flow, J. Fluids Struct. 19 (2004) 32l–334.
[17] K. Lam, F.H. Wang, R.M.C. So, Three-dimensional nature of vortices in the near wake of a wavy cylinder, J. Fluids Struct. 19 (2004) 815–833.
[18] W. Zhang, Daichin, S. Lee, PIV measurements of the near-wake behind a sinusoidal cylinder, Exp. Fluids 38 (2005) 824–832.
[19] S. Lee, A.T. Nguyen, Experimental investigation on wake behind a wavy cylinder having sinusoidal cross-sectional area variation, Fluid Dyn. Res. 39 (2007) 292–304.
[20] J. Kim, P. Moin, Application of a fractional step method to incompressible Navier–Stokes equations, J. Comput. Phys. 59 (1985) 308–323.
[21] Y. Zang, R.L. Street, J.R. Koseff, A non-staggered grid, fractional step method for time-dependent incompressible Navier–Stokes equations in curvilinear coordinates, J. Comput. Phys. 114 (1994) 18–33.
[22] J. Kim, D. Kim, H. Choi, An immersed-boundary finite volume method for simulations of flow in complex geometries, J. Comput. Phys. 171 (2001) 132–150.
[23] J. Kim, H. Choi, An immersed-boundary finite-volume method for simulation of heat transfer in complex geometries, KSME Int. J. 18 (2004) 1026–1035.
[24] J. Kim, H. Choi, Distributed forcing of flow over a circular cylinder, Phys. Fluids 17 (2005).
[25] A.G. Kravchenko, P. Moin, K. Shariff, B-spline method and zonal grids for simulations of complex turbulent flows, J. Comput. Phys. 151 (1999) 757–789.
[26] O. Posdziech, R. Grundmann, Numerical simulation of the flow around an infinitely long circular cylinder in the transition regime, Theor. Comput. Fluid Dyn. 15 (2001) 121–141.
[27] S.W. Churchill, M. Bernstein, A correlating equation for forced convection from gases and liquids to a circular cylinder in crossflow, J. Heat Transf. 99 (1997) 300–306.